Schmid, Daniel R.; Stiller, Peter L.; Dirnaichner, Alois; Huttel, Andreas K.

From Transparent Conduction to Coulomb Blockade at Fixed Hole Number

From Transparent Conduction to Coulomb Blockade at Fixed Hole Number

Daniel R. Schmid, Peter L. Stiller, Alois Dirnaichner, and Andreas K. Hüttel*

A complex set of transport spectroscopy data on a clean single-wall carbon nanotube device in high magnetic fields is presented. At zero axial field, the device displays in hole conduction with increasingly negative gate voltage a fast transition toward high contact transparency and eventually Fabry–Pérot interference of conductance. When increasing the axial field component up to $B_\parallel = 17$ T, the contact transparency and the overall conductance are reduced all the way to Coulomb blockade, clearly displaying the subsequent charging with the first ten holes. The continuous transition between the transport regimes is dominated by a rich spectrum of Kondo-like resonances, with distinct features in the stability diagrams.

1. Introduction

Carbon nanotubes provide a prototypical, highly versatile system for quantum transport, which has been the topic of extensive research over the last decades.[1] They have allowed the observation of electronic transport regimes as different as Coulomb blockade,[2,3] Kondo effect-dominated tunneling,[4,5] and electronic Fabry–Pérot interference.[6,7] A striking property of suspended, so-called "ultraclean" nanotube devices[3,8] is that the effective transparency of contacts can be tuned over a large range by application of a gate voltage alone, while maintaining the regularity of the confinement potential. In combination with analysis of the repetitive shell filling, this has led to studies on the evolution of transport regimes with tunnel coupling.[9–11]

When the absolute number of electrons or holes, as opposed to the shell filling, is relevant, investigating the dependence of the

Dr. D. R. Schmid, Dr. P. L. Stiller, Dr. A. Dirnaichner, Dr. A. K. Hüttel
Institute for Experimental and Applied Physics
University of Regensburg
93040 Regensburg, Germany
E-mail: andreas.huettel@ur.de

Dr. A. K. Hüttel
Low Temperature Laboratory
Department of Applied Physics
Aalto University
P.O. Box 15100, 00076 Aalto, Finland

The ORCID identification number(s) for the author(s) of this article can be found under https://doi.org/10.1002/pssb.202000253.

spectrum on barrier transparencies becomes more challenging. Approaches that have been pursued here include comparing hole and electron spectrum[12] (which utilizes electron–hole symmetry) or introducing additional barrier gates[13] (which requires more complex fabrication).

Here, we present data on the transport spectrum in the few-hole regime, where the contacts are transparent and typically a transition to Fabry–Pérot interference of conductance is observed.[6,7] Application of an axial magnetic field of up to $B_\parallel = 17$ T reduces the conductance in our device, leading via multiple Kondo-like transport resonances[4,5,14–16] all the way to strong Coulomb blockade, at a then known number of holes in the valence band. A comprehensive theoretical model for the data is so far still missing; however, we hope to inspire corresponding work. To facilitate this, the raw data of the measurements presented here is deposited online under an open access license.[17]

2. Device and Measurement

The inset of **Figure 1** displays a schematic of the measured device. Using chemical vapor deposition (CVD),[18] a carbon nanotube has been grown in situ across predefined, 40 nm thick rhenium contacts and a trench between them; the highly doped silicon chip substrate is used as a global back gate. The contact distance, as approximation for the suspended length of the nanotube segment, is $L = 700$ nm. During the CVD process, the contact metal surface is saturated with carbon;[19] barely any traces of superconductivity in the contacts can be found in the transport measurements.

The device was very stable, surviving multiple cool-downs in different cryostats with only minor changes, and very clean in the sense of highly regular transport spectra. Its characteristics in parameter ranges other than discussed here have already been presented in several publications.[3,5,20–22] The device shows the typical behavior of a small-bandgap carbon nanotube. For positive gate voltages $V_g > 0.6$ V, i.e., in electron conduction, strong Coulomb blockade with a repetitive shell filling pattern can be observed (not shown); the tunnel barriers here are formed by a wide p–n junction within the carbon nanotube.[3,23,24] The electronic bandgap is observed at a low positive gate voltage.

Figure 1a–c shows pre-characterization measurements of hole transport, for $V_g < 0.5$ V, performed in the vacuum of a helium-3 cryostat at $T \simeq 300$ mK. The differential conductance $G(V_g, V_{sd})$ as function of gate voltage V_g and bias voltage V_{sd}
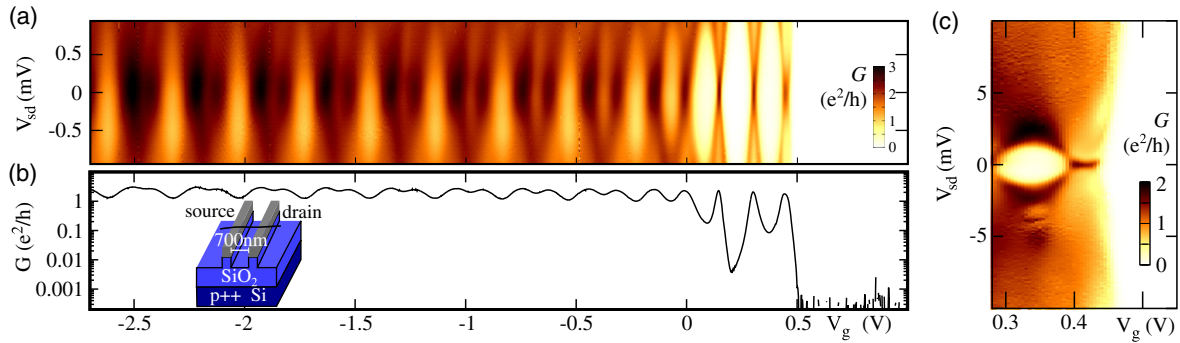
Figure 1. Inset: Sketch (not to scale) of the central part of the nanotube device, with a suspended carbon nanotube grown in situ across rhenium contacts. a) Differential conductance $G(V_{sd}, V_g)$ in the few-hole region, numerically differentiated from a DC current measurement; pre-characterization measurement at $T \simeq 300\,mK$. b) Zero DC bias conductance $G(V_g)$ as function of gate voltage V_g; trace cut from the data of (a). c) Differential conductance $G(V_{sd}, V_g)$ near the bandgap edge, from a detail DC current measurement for increased bias range and gate resolution; $T \simeq 300\,mK$.

is plotted in Figure 1a. While at this temperature close to the bandgap edge Coulomb blockade related effects are still visible, the transition into electronic Fabry–Pérot interference with a strongly broadened, oscillatory pattern and a conductance always exceeding $G_0 = e^2/h$[11] is clear for $V_g \ll 0\,V$. This is also demonstrated by the zero bias conductance trace plotted in Figure 1b, which shows a behavior strongly resembling, e.g., data published in ref. [7], including the onset of a Sagnac interference-induced modulation.

On closer observation, the precise nature of the conductance oscillations near the electronic bandgap already turns out to be more complex than expected. Figure 1c shows a detail measurement of the rapid conductance onset at the gap edge. The measurement exhibits no indications of further structure within the gap region even at high bias, strong filtering and wide-range logarithmic color scale plotting, indicating that the nanotube is here fully depleted of free carriers. The first electron enters the conductance band at $V_g \simeq 0.68\,V$ with a sharp Coulomb oscillation (not shown). Conversely, the low-bias conductance maximum near $V_g = 0.4\,V$ resolves into a structure broadly extended in V_g, allowing for speculation that it represents a Kondo ridge with already the addition of two holes.[4,5]

3. Large Axial Magnetic Field

In the following, all presented data has been recorded at base temperature $T \simeq 30\,mK$ of a top-loading dilution refrigerator, with the device immersed into the diluted phase of the liquid $^3He/^4He$ mixture. The dilution refrigerator was equipped with a 17 T superconducting magnet and a rotateable sample holder, such that the relative orientation of the magnetic field and the carbon nanotube could be adjusted within the chip surface plane.

Our central observation is shown in **Figure 2**. It plots the zero-bias conductance $G(B_\parallel, V_g)$ in the few-hole regime, as function of both gate voltage V_g and magnetic field in the direction of the carbon nanotube axis $B_\parallel$, over a wide field range $0\,T \leq B_\parallel \leq 17\,T$.

At low magnetic field, left edge of the plot, the transition toward Fabry–Pérot interference[6,7] with an overall increasing conductance is visible. For further clarity, the conductance trace $G(0\,T, V_g)$ of the data set has been overlaid as a white line plot; G exceeds $3e^2/h$ around $V_g = -0.2\,V$. It shows several oscillations;
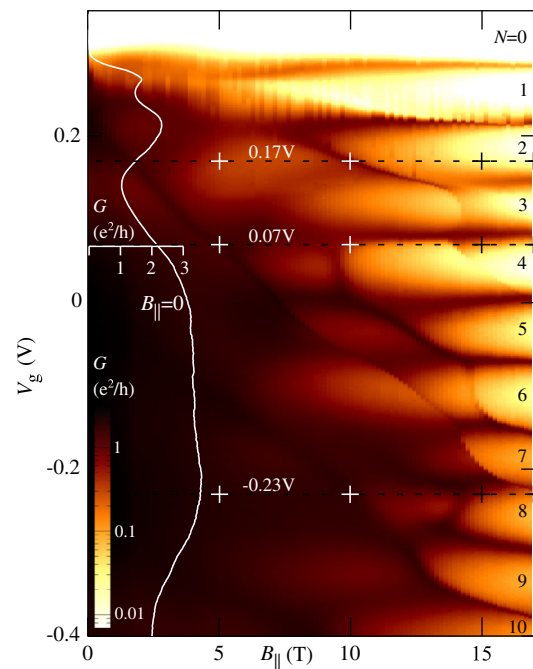

Figure 2. Zero bias conductance $G(B_\parallel, V_g)$ in the few-hole regime at dilution refrigerator base temperature $T \simeq 30\,mK$, as function of gate voltage V_g and magnetic field $B_\parallel$ parallel to the carbon nanotube axis. Absolute hole numbers at large field are indicated by numbers at the right graph edge. The overlaid line trace plots the conductance at $B_\parallel = 0$ (same V_g axis). Dashed lines and crosses mark the parameters of the trace cuts in Figure 4.

comparing the gate voltage scale of the broad ridge in the region $-0.3\,V \leq V_g \leq 0\,V$ with the high field behavior discussed below and with Figure 1 indicates that we observe here already a $4e$-periodic phenomenon, at the transition between SU(4) Kondo effect and Fabry–Pérot interference.[11]

Conversely, at high axial magnetic field, up to $B_\parallel = 17\,T$ at the right edge of the plot, the overall conductance is significantly lower, and the nanotube device displays well-separated Coulomb oscillations of conductance. A careful search at the edge of the bandgap region has not shown any indications of

ADVANCED
SCIENCE NEWS

www.advancedsciencenews.com

pssb
physica status solidi b

www.pss-b.com

further features in hole conductance at more positive V_g. This allows to identify the absolute number of holes N in the system in Coulomb blockade; see the numbers at the right edge of the plot.

The transition from transparent conductance to Coulomb blockade behavior, filling the central area of the plot, displays an extraordinary degree of complexity. Kondo-like resonances cross Coulomb blockade areas, with different levels of background (cotunneling) conductance on either side of them. They merge into diagonal features in the plot, for lower field passing to more positive gate voltages. From a theory perspective, the transition has to involve a reduction of the charging energy per hole from being the dominant energy scale to nearly zero, giving an indication of the expected multitude of phenomena.

Extending the data of Figure 2, **Figure 3** plots stability diagrams, i.e., the differential conductance $G(V_{sd}, V_g)$ as function of bias voltage V_{sd} and gate voltage V_g, for fixed values of the magnetic field $B_\parallel$ in each panel. At comparatively low magnetic field $B_\parallel = 5\,T$, only strongly broadened patterns can be observed; see Figure 3a. At $B_\parallel = 10\,T$, Figure 3b, first features resembling diamond-shaped Coulomb blockade regions emerge. They are strongly distorted and broadened, overlaid by a wide zero-bias ridge of enhanced conductance at $V_g \simeq -0.2\,V$, and by strongly bias-dependent resonances as, e.g., at $V_g \simeq 0.17\,V$. The trend toward lower conductance and more regular Columb blockade regions continues with $B_\parallel = 15\,T$, Figure 3c, where except for the region near $V_g \simeq -0.25\,V$ the zero-bias conductance anomalies are nearly gone, and $B_\parallel = 17\,T$, Figure 3d.

4. Detail Observations

To gain insight into the nature of the "diagonally running resonances" in the magnetoconductance spectrum of Figure 2, in **Figure 4**, we plot selected line traces both from Figure 2

and 3. We chose gate voltages such that at the magnetic fields $B_\parallel$ of the stability diagrams of Figure 3 such a resonance is observed. The corresponding gate voltages are marked in Figure 2 and 3 with dashed lines.

For the first two panels, Figure 4a,b, the gate voltage is $V_g = 0.17\,V$; at this voltage, a resonance crosses $B_\parallel = 10\,T$; see the white cross in Figure 2. This resonance becomes clearly visible again in the line cut of Figure 4a as a distinct local maximum of conductance. Figure 4b shows the corresponding bias traces of the panels of Figure 3, at $B_\parallel = 5, 10, 15, 17\,T$. The trace at $B_\parallel = 10\,T$ immediately stands out with a (near) zero bias anomaly of conductance, suggesting a Kondo-like behavior of the observed phenomenon. Surprisingly, the conductance maximum displays a strong gate voltage dependence in Figure 3b.

Similar behavior of the line traces is observed in Figure 4c,d at $B_\parallel = 5\,T$ and in Figure 4e,f at $B_\parallel = 10\,T$. For Figure 4c,d, $B_\parallel = 5\,T$ and $V_g \simeq 0.07\,V$, the corresponding region in the stability diagram of Figure 3a resembles a Coulomb blockade degeneracy point; it also evolves at higher magnetic field into the $3 \leq N \leq 4$ transition. In the case of Figure 4e,f at $B_\parallel = 10\,T$ and $V_g \simeq -0.23\,V$, the zero-bias conductance maximum corresponds to a wide region in Figure 3b similar to merged Kondo ridges. In addition, in the latter panels, also the conductance feature near but not exactly at $B_\parallel = 15\,T$ translates into a conductance maximum in bias dependence. Note that the data indicates a global shift of all features in bias on the order of $\Delta V_{sd} \sim +0.1\,meV$, most likely due to an input offset of the current amplifier. On close observation the same offset is also visible in Figure 3.

A surprising detail of the stability diagrams of Figure 3 is the presence of several sickle-shaped features of positive, low, or even strong negative differential conductance; see the arrows in the figure. Two of the corresponding regions are enlarged in **Figure 5**, each accompanied by the simultaneously measured DC current.
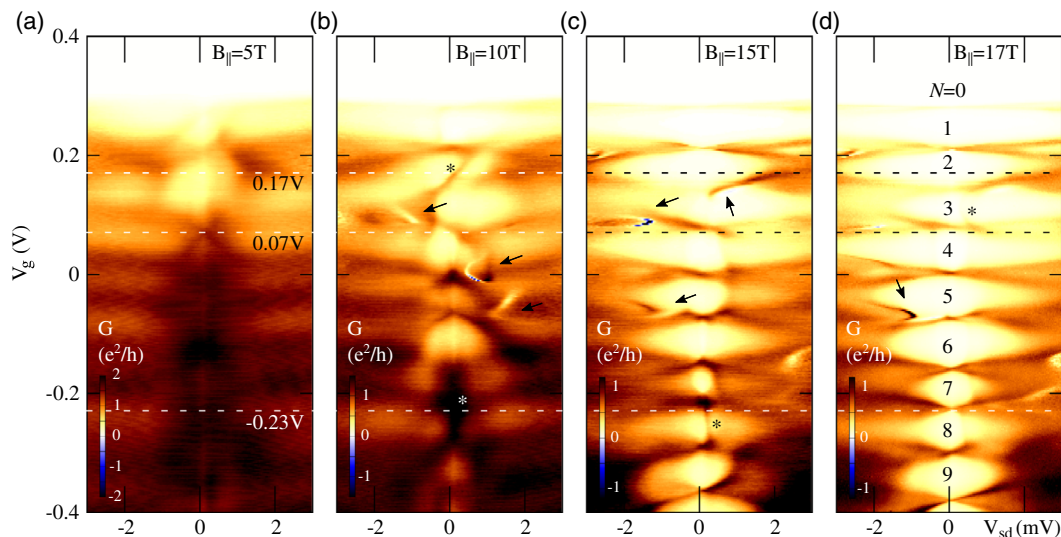

Figure 3. Stability diagrams, plotting the differential conductance $G(V_{sd}, V_g)$ as function of bias voltage V_{sd} and gate voltage V_g, for fixed magnetic field parallel to the cabon nanotube axis: a) $B_\parallel = 5\,T$, b) $B_\parallel = 10\,T$, c) $B_\parallel = 15\,T$, d) $B_\parallel = 17\,T$. Negative differential conductance is plotted in blue. The dashed lines mark the gate voltage values of the trace cuts in Figure 4. Asterisks indicate Kondo-like low-bias anomalies of conductance, arrows sickle-shaped features; see the text.
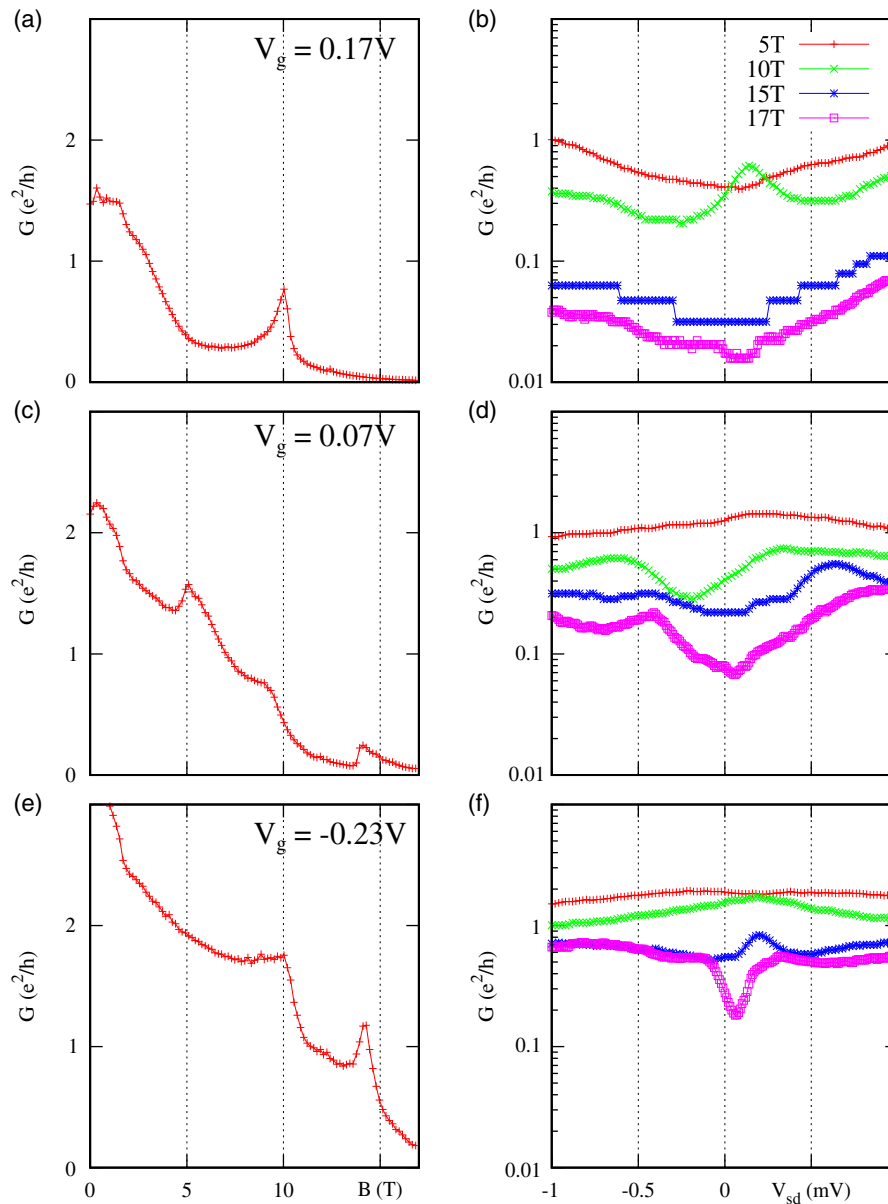
Figure 4. Conductance traces for fixed gate voltage a,b) $V_g = 0.17\,V$, c,d) $V_g = 0.07\,V$, and e,f) $V_g = -0.23\,V$. a,c,e) Trace cuts from Figure 2, plotting the differential conductance $G(B_\parallel)$ as function of parallel magnetic field, at constant $V_{sd} \simeq 0$. b,d,f) The corresponding sections of the panels of Figure 3, plotting the conductance $G(V_{sd})$ as function of bias, for constant $B_\parallel = 5, 10, 15, 17\,T$. In (b), the lock-in amplifier reached its resolution limit in the 15 T trace, leading to step-like measurement artifacts.

The precise origin of these features is unknown; their shape does not correspond to typical single electron tunneling or cotunnelling phenomena. Given that the measurement took place with the device immersed in liquid helium, and that a high magnetic field was present, mechanical self-activation is unlikely to be the cause.[20,21,25–27] A self-driving mechanism would need to overcome both viscous damping and dissipation due to induction. An unambiguous decision whether the sharpest such features here in our measurement are sudden switching events, as expected for the onset of mechanical instability, is not possible from the data set due to the averaging times of lock-in amplifier

and multimeter. Some of the sickle-shaped features in Figure 3 are, however, clearly broadened; see, e.g., the region enlarged in Figure 5c,d, also speaking against a vibrational instability phenomenon.

5. Further Data

In **Figure 6**a, the magnetic field is kept constant at its maximum value, $B = 17\,T$, but the sample holder is rotated stepwise; the magnetic field remains in the chip surface plane, but the relative
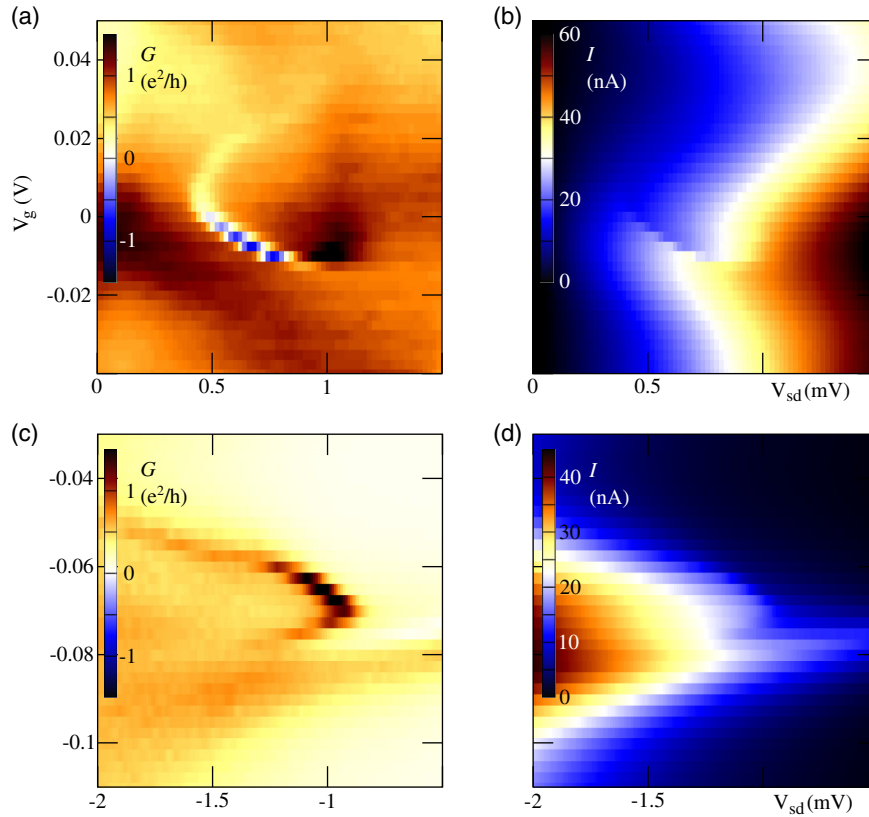
Figure 5. a) Detail enlargement of the differential conductance measurement $G(V_{sd}, V_g)$ of Figure 3b; $B_\parallel = 10\,\text{T}$. b) Simultaneously measured dc current $I(V_{sd}, V_g)$. c) Detail enlargement of the differential conductance measurement $G(V_{sd}, V_g)$ of Figure 3d; $B_\parallel = 17\,\text{T}$. d) Simultaneously measured DC current $I(V_{sd}, V_g)$.
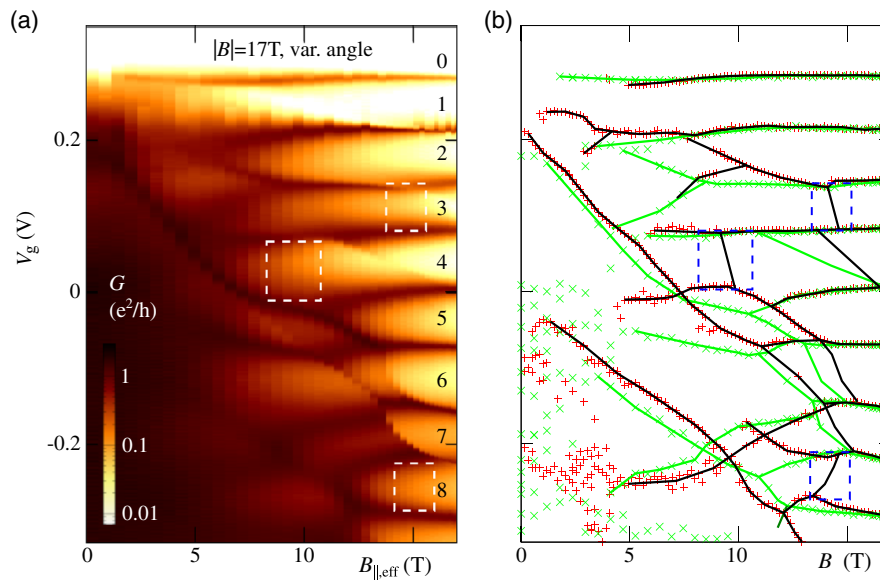

Figure 6. a) Zero bias conductance $G(B_{\parallel,\text{eff}}, V_g)$ as function of gate voltage V_g and effective axial magnetic field $B_{\parallel,\text{eff}} = B\cos(\phi)$, for constant $B = 17\,\text{T}$ and varied angle ϕ between nanotube axis and field direction. The dashed white rectangles mark regions where the pattern clearly deviates from Figure 2. b) Points: automatically extracted local maxima of the $G(V_g)$ traces of the datasets of Figure 2 and 6a; solid lines: manually inserted guides to the eye, also considering step-like features. Red points/black lines: varied parallel field, data of Figure 2; green points/green lines: rotating device in constant field, data of Figure 6a.

orientation of nanotube axis and field changes. The plot shows the differential conductance as function of gate voltage and axial magnetic field component $B_{\parallel,\mathrm{eff}} = B\cos(\phi)$, with ϕ as the angle between field direction and nanotube axis. The overall similarity between Figure 6a and 2 immediately confirms that the axial field component is crucial for the suppression of overall conductance and for most of the observed spectrum features. On closer observation, however, there are subtle deviations in the conductance resonance pattern between the figures, indicating that the large angle-independent Zeeman energy here modifies the transport spectrum. Three particularly clear cases where resonance lines visible in Figure 2 are absent in Figure 6a are marked with dashed rectangles in the figure.

Figure 6b explicitly compares the two measurements. Local maxima have been extracted from $G(V_g)$ traces and plotted as points; based on these points, lines have been drawn manually to connect them, also considering step-like features in the data that did not trigger the maximum search. As last step, the two sets of points and lines have been superimposed. Red points and black lines stem from the data of Figure 2, where an axial magnetic field of varied strength is applied; green points and green lines stem from Figure 6a, where at fixed magnetic field value $B = 17\,\mathrm{T}$ the angle ϕ between nanotube and field and with that the axial component is varied. As expected, at the right edge of the plot, with $B_{\parallel} = 17\,\mathrm{T}$ (or $\phi = 0$) the patterns coincide. For smaller field or larger angle, the deviations gradually increase; the three resonances missing in Figure 6a are marked again with dashed lines.

Figure 7a plots the conductance in the case of a magnetic field perpendicular to the nanotube axis, $G(B_{\perp}, V_g)$. The overall signal remains large, and only broad features occur. Around zero magnetic field, a gate voltage independent pattern of larger conductance is visible, which may be related to superconductivity in the rhenium contacts.

Finally, Figure 7b shows a detail measurement at low parallel magnetic field $-1\,\mathrm{T} \leq B_{\parallel} \leq 2\,\mathrm{T}$. Again, around zero field, larger

conductance is observed, consistent with an impact of the contact metal independent of the precise in-plane orientation of the magnetic field.

6. Discussion

Although significant research has been published regarding carbon nanotubes grown in situ over metal contacts, the precise interface properties and contact geometries in low-temperature experiments still pose open questions. In the case of electron transport, quantum dot confinement is typically given by an electrostatically induced p–n junction within the nanotube, and the contacts to the quantum dot are formed by segments of the nanotube itself beyond these junctions. The nanotube–metal interface can be treated as small perturbation or even neglected.[3,23] This is, however, not the case for hole transport (i.e., negative applied gate voltages), where the p–n junction is absent.

Regarding the overall suppression of conductance with increasing axial magnetic field, it has been demonstrated recently that cross-quantization affects in such a field the shape of electronic wave functions along the carbon nanotube axis.[3,22] This leads to smaller tunnel rates to the contacts in the high field limit. The observation in ref. [3] and the corresponding theoretical analysis was, however, targeted at the case of single electron states in a well-closed off system. It may require extension or modification for transparent contacts and interacting charges.

In ref. [28], also an impact of a magnetic field on the tunnel coupling is discussed, though state-specific for KK'-mixed doublet states and on a smaller magnetic field scale. The mechanism proposed in ref. [28] is that the axial field modifies the circumferential wave function and with that the wavefunction overlap at a side contact. Given that in our device the nanotube lies on top of the contacts, this may well be relevant specifically in the hole regime.

Regarding carbon nanotube transport spectra in magnetic fields, many works have demonstrated complex results including
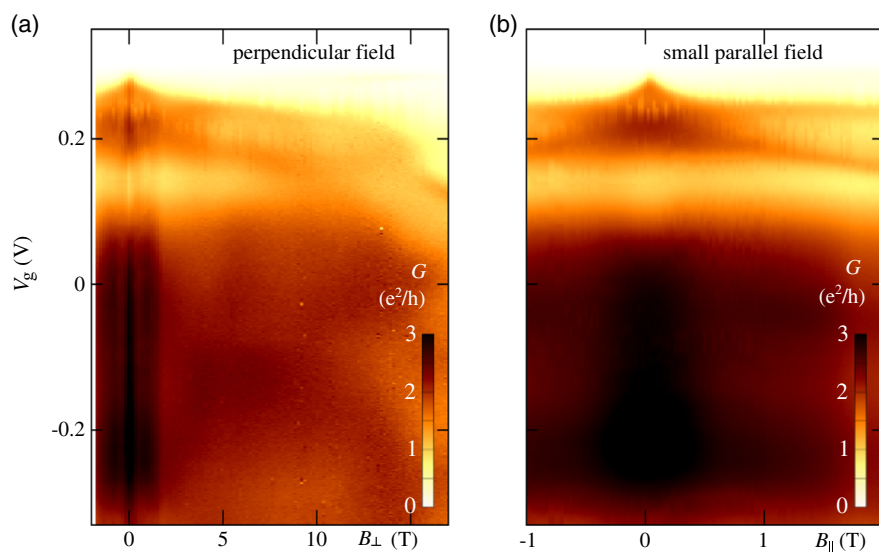

Figure 7. a) Conductance $G(B_{\perp}, V_g)$ as function of gate voltage V_g and magnetic field $B_{\perp}$ perpendicular to the nanotube axis. b) Conductance $G(B_{\parallel}, V_g)$ as function of gate voltage V_g and magnetic field $B_{\parallel}$ parallel to the nanotube axis, in higher resolution for the low-field range $-1\,\mathrm{T} \leq B_{\parallel} \leq 2\,\mathrm{T}$.

multiple ground state transitions as well as, e.g., Kondo phenomena caused by nontrivial degeneracies.[15,16,28–30] The gradual transition between transport regimes has been studied mostly via the impact of a changing gate voltage on a repetitive shell-filling pattern in linear response.[9–11,31,32] This has allowed to observe and model the emergence of the Kondo effect in its SU(2) and SU(4) manifestation and the transition between Coulomb blockade and Fabry–Pérot oscillations.[10,11] The interplay of Kondo transport, where on-site repulsion (i.e., charging energy) is still relevant, and quantum interference in an open system however still poses conceptual challenges, recently leading to the proposal of "correlated Fabry–Pérot oscillations" in the transition regime.[11]

Finally, features quite similar to the diagonal lines of Figure 2 can be found in ref. [28]; see Figure 3c there. The authors describe their observations as cotunneling corresponding to magnetic-field-induced level crossings; a functional renormalization group calculation is used to successfully model many details of their measurements. Similar approaches may be able to cover at least part of the parameter range of our data shown in Figure 2.

7. Conclusion

We present millikelvin transport spectroscopy measurements on a well-characterized carbon nanotube device,[3,5,20,21] where in a strong axial magnetic field $B_\parallel \leq 17\,T$ the entire range of transport regimes from transparent conduction to Coulomb blockade can be traced at well-known absolute hole number. A multitude of quantum ground state transitions and Kondo-like resonances emerges in the interacting few-hole system. Although similar phenomena have been observed and analyzed for smaller parameter spaces in literature, see, e.g., ref. [28], a theoretical description covering strong Coulomb blockade, the Kondo regime, as well as quantum interference in an open conductor in a consistent way is still lacking. Our raw data is available to the interested reader[17] (for the used open source measurement package, see ref. [33]); we hope to inspire corresponding work.

Conflict of Interest

The authors declare no conflict of interest.

[1] E. A. Laird, F. Kuemmeth, G. A. Steele, K. Grove-Rasmussen, J. Nygård, K. Flensberg, L. P. Kouwenhoven, *Rev. Mod. Phys.* **2015**, *87*, 703.

[2] S. J. Tans, M. H. Devoret, H. Dai, A. Thess, R. E. Smalley, L. J. Geerligs, C. Dekker, *Nature* **1997**, *386*, 474.

[3] M. Margańska, D. R. Schmid, A. Dirnaichner, P. L. Stiller, C. Strunk, M. Grifoni, A. K. Hüttel, *Phys. Rev. Lett.* **2019**, *122*, 086802.

[4] J. Nygård, H. C. Cobden, P. E. Lindelof, *Nature* **2000**, *408*, 342.

[5] K. J. G. Götz, D. R. Schmid, F. J. Schupp, P. L. Stiller, C. Strunk, A. K. Hüttel, *Phys. Rev. Lett.* **2018**, *120*, 246802.

[6] W. Liang, M. Bockrath, D. Bozovic, J. H. Hafner, M. Tinkham, H. Park, *Nature* **2001**, *411*, 665.

[7] A. Dirnaichner, M. del Valle, K. J. G. Götz, F. J. Schupp, N. Paradiso, M. Grifoni, C. Strunk, A. K. Hüttel, *Phys. Rev. Lett.* **2016**, *117*, 166804.

[8] J. Cao, Q. Wang, H. Dai, *Nat. Mater.* **2005**, *4*, 745.

[9] A. Makarovski, J. Liu, G. Finkelstein, *Phys. Rev. Lett.* **2007**, *99*, 066801.

[10] F. B. Anders, D. E. Logan, M. R. Galpin, G. Finkelstein, *Phys. Rev. Lett.* **2008**, *100*, 086809.

[11] W. Yang, C. Urgell, S. L. De Bonis, M. Marganska, M. Grifoni, A. Bachtold, *Phys. Rev. Lett.* **2020**, *125*, 187701.

[12] M. Niklas, S. Smirnov, D. Mantelli, M. Marganska, N. V. Nguyen, W. Wernsdorfer, J. P. Cleuziou, M. Grifoni, *Nat. Commun.* **2016**, *7*, 12442.

[13] A. Benyamini, A. Hamo, S. V. Kusminskiy, F. von Oppen, S. Ilani, *Nat. Phys.* **2014**, *10*, 151.

[14] D. Goldhaber-Gordon, H. Shtrikman, D. Mahalu, D. Abusch-Magder, U. Meirav, M. A. Kastner, *Nature* **1998**, *391*, 156.

[15] P. Jarillo-Herrero, J. Kong, H. S. J. van der Zant, C. Dekker, L. P. Kouwenhoven, S. De Franceschi, *Nature* **2005**, *434*, 484.

[16] D. R. Schmid, S. Smirnov, M. Margańska, A. Dirnaichner, P. L. Stiller, M. Grifoni, A. K. Hüttel, C. Strunk, *Phys. Rev. B* **2015**, *91*, 155435.

[17] D. R. Schmid, P. L. Stiller, A. Dirnaichner, A. K. Hüttel, Raw data for "From Transparent Conduction to Coulomb Blockade at Fixed Hole Number", Zenodo, **2020**, https://doi.org/10.5281/zenodo.4037354.

[18] J. Kong, H. T. Soh, A. M. Cassell, C. F. Quate, H. Dai, *Nature* **1998**, *395*, 878.

[19] K. J. G. Götz, S. Blien, P. L. Stiller, O. Vavra, T. Mayer, T. Huber, T. N. G. Meier, M. Kronseder, C. Strunk, A. K. Hüttel, *Nanotechnology* **2016**, *27*, 135202.

[20] D. R. Schmid, P. L. Stiller, C. Strunk, A. K. Hüttel, *New J. Phys.* **2012**, *14*, 083024.

[21] D. R. Schmid, P. L. Stiller, C. Strunk, A. K. Hüttel, *Appl. Phys. Lett.* **2015**, *107*, 123110.

[22] P. L. Stiller, A. Dirnaichner, D. R. Schmid, A. K. Hüttel, *Phys. Rev. B* **2020**, *102*, 115408.

[23] J. Park, P. L. McEuen, *Appl. Phys. Lett.* **2001**, *79*, 1363.

[24] F. Kuemmeth, S. Ilani, D. C. Ralph, P. L. McEuen, *Nature* **2008**, *452*, 448.

[25] G. A. Steele, A. K. Hüttel, B. Witkamp, M. Poot, H. B. Meerwaldt, L. P. Kouwenhoven, H. S. J. van der Zant, *Science* **2009**, *325*, 1103.

[26] Y. Wen, N. Ares, F. J. Schupp, T. Pei, G. A. D. Briggs, E. A. Laird, *Nat. Phys.* **2020**, *16*, 75.

[27] C. Urgell, W. Yang, S. L. De Bonis, C. Samanta, M. J. Esplandiu, Q. Dong, Y. Jin, A. Bachtold, *Nat. Phys.* **2020**, *16*, 32.

[28] K. Grove-Rasmussen, S. Grap, J. Paaske, K. Flensberg, S. Andergassen, V. Meden, H. I. Jørgensen, K. Muraki, T. Fujisawa, *Phys. Rev. Lett.* **2012**, *108*, 176802.

[29] P. Jarillo-Herrero, J. Kong, H. S. J. van der Zant, C. Dekker, L. P. Kouwenhoven, S. De Franceschi, *Phys. Rev. Lett.* **2005**, *94*, 156802.

[30] V. Deshpande, M. Bockrath, *Nat. Phys.* **2008**, *4*, 314.

[31] B. Babić, C. Schönenberger, *Phys. Rev. B* **2004**, *70*, 195408.

[32] A. Makarovski, A. Zhukov, J. Liu, G. Finkelstein, *Phys. Rev. B* **2007**, *75*, 241407.

[33] S. Reinhardt, C. Butschkow, S. Geissler, A. Dirnaichner, F. Olbrich, C. Lane, D. Schröer, A. K. Hüttel, *Comput. Phys. Commun.* **2019**, *234*, 216.